Resonant alignment of microswimmer trajectories in oscillatory shear flows

Alexander Hope,[1] Ottavio A. Croze,[2, *] Wilson C. K. Poon,[3] Martin A. Bees,[4] and Mark D. Haw[1]

[1]*Department of Chemical and Process Engineering, University of Strathclyde,*
James Weir Building, 75 Montrose Street, Glasgow G1 1XJ, United Kingdom
[2]*Cavendish Laboratory, University of Cambridge, Cambridge, CB3 0HE, United Kingdom*
[3]*SUPA and The School of Physics & Astronomy, The University of Edinburgh,*
Kings Buildings, Mayfield Road, Edinburgh EH9 3JZ, United Kingdom
[4]*Department of Mathematics, University of York, York YO10 5DD, United Kingdom*
(Dated: February 6, 2017)

Oscillatory flows are commonly experienced by swimming microorganisms in the environment, industrial applications and rheological investigations. We experimentally characterise the response of the alga *Dunaliella salina* to oscillatory shear flows, and report the surprising discovery that algal swimming trajectories orient perpendicular to the flow-shear plane. The ordering has the characteristics of a resonance in the driving parameter space. The behaviour is qualitatively reproduced by a simple model and simulations accounting for helical swimming, suggesting a mechanism for ordering and criteria for the resonant amplitude and frequency. The implications of this work for active oscillatory rheology and industrial algal processing are discussed.

PACS numbers: Valid PACS appear here

Many swimming microorganisms experience shear flow in natural and industrial processes. Swimming is strongly biased by environmental cues and fluid shear [1, 2], with significant implications for ecology [3] and industrial exploitation [4]. Classic examples include directed swimming relative to light (phototaxis) and hydrodynamic focusing in down-welling flow due to viscous and gravitational torques (gyrotaxis) [1, 5].

There is great potential to use individual and collective microswimmer behaviour to improve microbial biotechnology, such as algal photobioreactor design [4]. For example, gyrotactic microorganisms in laminar channel flow tend to focus and so drift faster and diffuse less than non-swimming cells or nutrients [6, 7] while in turbulent flows cells accumulate in transiently downwelling [7–9] or strongly accelerated [10] regions. Horizontal shear flows can trap gyrotactic swimmers (a mechanism for oceanic thin layers) [3] and modify hydrodynamic instabilites and patterns (bioconvection) [11, 12]. Phototaxis and shear flow can combine to drive cell focusing [13] and pattern formation [14]. Complex transport dynamics can even result from relatively simple shear flow [2, 15]. The rheology of active media is also of recent interest: suspensions of swimming bacteria behave less viscously [16] and algae more viscously [17] than dead cells.

Here, we investigate the interaction of the swimming alga *Dunaliella salina* with oscillatory shear flows. Surprisingly, in experiments swimming trajectories are strongly ordered by the flow for particular driving parameter values. The ordering mechanism is distinct from that observed recently with *Dunaliella primolecta*, with constant, strong shear flows [18]. We explore the observed resonant ordering employing simple but predictive models, and discuss implications for active oscillatory rheology and industrial processing of swimming algae.
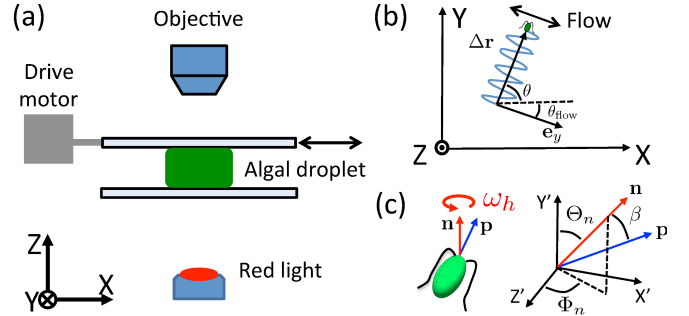

FIG. 1. (a) Oscillatory flow and imaging setup. (b) Trajectories orientations θ from the x-axis are evaluated from their displacements $\Delta \mathbf{r}$. The flow axis $\mathbf{e}_y$ was often rotated by θ_{flow} from x (consistent across repeat experiments). (c) *Dunaliella salina* swimming and helical rotation directions, $\mathbf{p}$ and $\mathbf{n}$; model coordinate system and angles (see text).

D. salina CCAP 19/18 cells (long axis $\approx 15\,\mu$m) were grown on modified Pick medium [19, 20] under 12:12 light/dark cycle at 21°C. All experiments were carried out at this temperature. Cells were concentrated by upswimming (gravitaxis) using cotton wool rafts [11]. Dilute (10^6 cells/ml) suspensions were subjected to oscillatory shear on the stage of an optical microscope (Olympus BX51). The suspension was placed between two transparent parallel plates 400 μm apart, the top plate connected to an electromechanical drive that sinusoidally sheared the suspension (Fig. 1). Plate parallelism was ensured by zeroing sample capillary flow. Video sequences (100-400 Hz) of sheared algae were acquired using a Mikrotron MC1310 at $10\times$ (NA 0.25) using red-filtered bright-field illumination to minimise phototaxis [21]. Sequences were captured in a plane equidistant from top and bottom plates at depth 200 μm. Algae were tracked using MATLAB versions of established

algorithms [22, 23]. The direction of the imposed oscillating flow was inferred from short-time cell trajectories and confirmed by tracking PEGylated polystyrene colloids (Supplementary Materials, Fig. S1). Cell observation before and after measurements found that the apparatus did not damage the cells (e.g. deflagellation).

With no flow, *D. salina* swimming trajectories were distributed isotropically in the horizontal plane (Fig. 2a). As in [24], gravitactic bias was not evident for tracks in this plane on experimental timescales. On application of oscillatory shear with amplitude A and frequency f trajectories might be expected simply to reflect superposition of isotropic swimming and oscillatory advection. This was indeed the case for some driving parameters, such as $A = 240$ μm and $f = 6$ Hz (Fig 2b). However, for $A = 448$ μm and $f = 2$ Hz swimming trajectories unexpectedly aligned perpendicular to the flow-shear plane (Fig. 2c). Alignment can be quantified by the start-to-end displacement, $\Delta\mathbf{r}(\tau)$, of each swimmer trajectory (Fig. 1b). Evaluated at short times within a cycle, $\Delta\mathbf{r}(\tau)$ provides the flow direction $\mathbf{e}_y \sim \Delta\mathbf{r}(\tau \to 0)$. However, evaluating $\Delta\mathbf{r}(\tau)$ over the largest available integer multiple n of the oscillation period, $\tau = n/f$, provides overall trajectory orientation, θ, and speed, $v_t = |\Delta\mathbf{r}|/\tau$.

Distributions $P(\theta)$ of orientations are presented beside the trajectories in Fig. 2. The distribution for $f = 2$ Hz, $A = 448$ μm shows how trajectories orient along the line perpendicular to the flow-shear plane, but are equally likely in either direction along this line. If the flow is halted, the distribution returns to uniform (Fig. S1, Supplementary Materials). Speed distributions for aligned trajectories (Fig. 2c) are similar to those without flow (Fig. 2a). These reflect the swimming speed distribution [25]. Hence, swimmers in aligned trajectories travel perpendicular to the flow at their swimming speed (but very slow swimmers cannot make much progress, biasing the distribution towards high speeds in Fig. 2c). Without alignment (Fig. 2b), the speed distribution reflects contributions by swimming and the oscillatory flow, which accounts for the bias towards low speeds.

To statistically quantify observed alignment as a function of the flow parameters, we count trajectories with displacement $\Delta\mathbf{r}$ oriented perpendicular, $N_\perp$, and parallel, $N_\parallel$, to the flow direction and define $R = N_\perp/N_\parallel$. By parallel (perpendicular) displacements we mean swimming orientations within $\pm\pi/4$ of the flow (vorticity) axis. We also provide the alternative measure $r = (\langle\sin(\theta - \theta_{flow})\rangle^2 + \langle\cos(\theta - \theta_{flow})\rangle^2)^{1/2} \in [0, 1]$, where averages are over all angles (which were doubled for axial distributions at resonance) [26]. Small r denotes isotropy, large r alignment (see Fig. 2). The surface plot in Fig. 3 illustrates how the alignment has the characteristics of resonance, occupying a small region of the imposed flow parameter space. Fixed amplitude and frequency sections of the ordering surface are shown in Fig. 4 and discussed below.
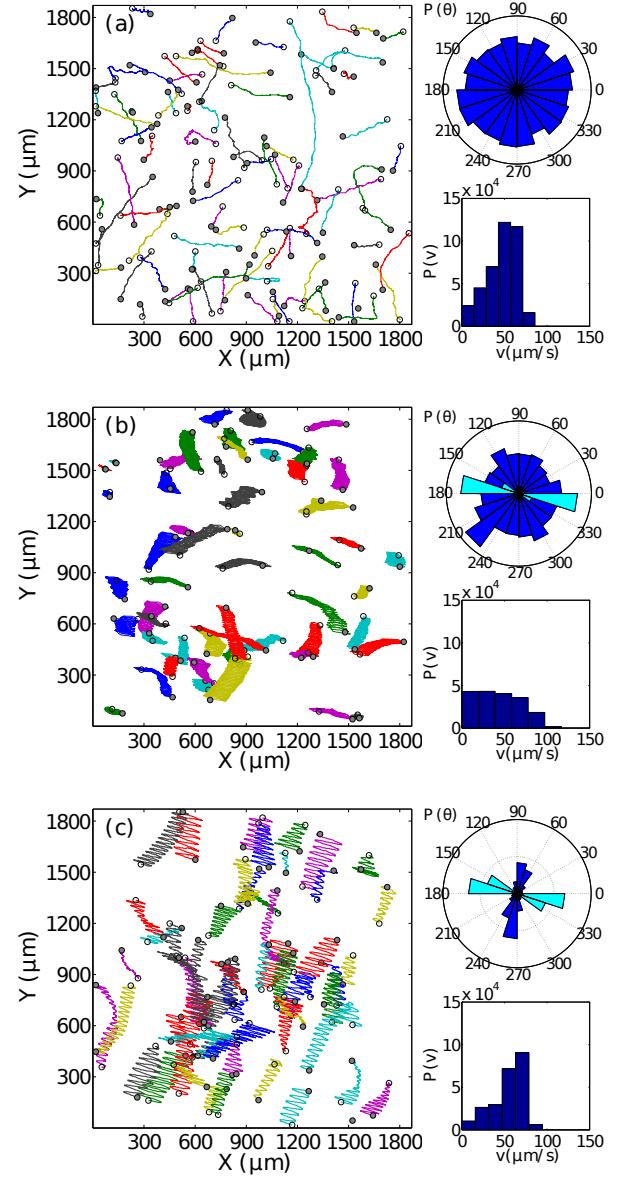

FIG. 2. Trajectories, orientation and speed distributions of *D. salina*. (a) No flow: isotropic trajectories (alignment measures $[r = 0.02, R = 0.9]$, see text). (b) Oscillatory shear flow with amplitude $A = 240$ μm and frequency $f = 6$ Hz: tracks show oscillation (cyan) at short times, but are isotropic (blue) at longer times $[r = 0.05, R = 1.6]$. (c) $A = 448$ μm and $f = 2$ Hz: swimming directions align perpendicular (blue) to the flow oscillation direction (cyan) $[r = 0.53, R = 4.4]$. Open/closed circles denote start/end points of each 2.5s track.

Discussion. The observed trajectories result from the combination of shear flow and swimming. Many algae swim helically, in part to facilitate phototaxis via a directional eyespot [27]. Thus we model the algae as helical swimmers in a flow. Following [28], we assume that a cell at position $\mathbf{r}$ swimming with speed v in direction $\mathbf{p}$ has an intrinsic angular velocity $\omega_h\mathbf{n}$ about an axis
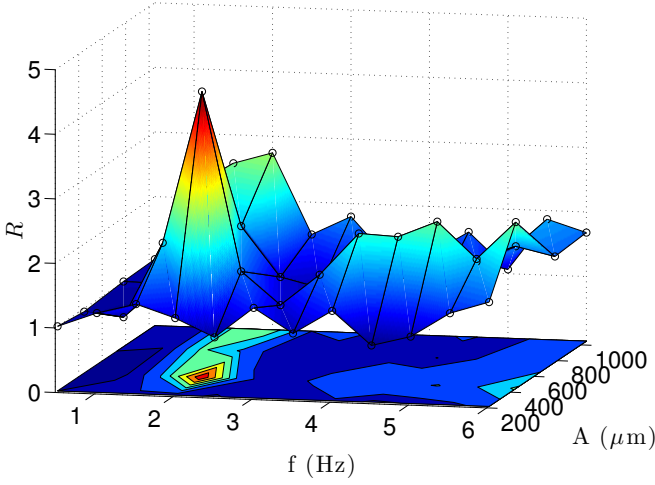
FIG. 3. Alignment ratio R as a function of driving amplitude A and frequency f for oscillatory flow in a shear cell with $H = 400\,\mu$m gap width. A is a measure of horizontal displacement.

$\mathbf{n}$, where $\mathbf{p} \cdot \mathbf{n} = \cos\beta$, for constant angle β, due to an asymmetric (non-planar) flagellar stroke. Hence, if the only external torque is due to flow with velocity $\mathbf{u}$ and vorticity $\boldsymbol{\omega}$, spherical swimmers obey $\dot{\mathbf{r}} = \mathbf{u}(t) + v\mathbf{p}$, $\dot{\mathbf{p}} = \left(\frac{1}{2}\boldsymbol{\omega}(t) + \omega_h\mathbf{n}\right) \times \mathbf{p}$ and $\dot{\mathbf{n}} = \frac{1}{2}\boldsymbol{\omega}(t) \times \mathbf{n}$. Experimental observations suggest that the fluid velocity is $\mathbf{u}(t) = \dot{\gamma}_\infty Z \cos(\omega_d t)\mathbf{e}_x$, with vorticity $\boldsymbol{\omega}(t) = \dot{\gamma}_\infty \cos(\omega_d t)\mathbf{e}_y$. Here $\mathbf{e}_x$ and $\mathbf{e}_y$ are along the positive flow and vorticity directions, respectively, $\dot{\gamma}_\infty = \omega_d A/H$ is the maximum shear rate and $\omega_d = 2\pi f$ is the angular driving frequency (recall A, f and H are driving amplitude, frequency and gap width, respectively). Nondimensionalising lengths with A and times with $1/\omega_d$, the model equations read

$$\dot{\mathbf{r}} = \Gamma \cos(t) Z\mathbf{e}_x + \nu\mathbf{p} \tag{1}$$

$$\dot{\mathbf{p}} = \left[\frac{\Gamma}{2}\cos(t)\mathbf{e}_y + \Omega^{-1}\mathbf{n}\right] \times \mathbf{p}; \;\; \dot{\mathbf{n}} = \frac{\Gamma}{2}\cos(t)\mathbf{e}_y \times \mathbf{n} \tag{2}$$

where $\Gamma = \dot{\gamma}_\infty/\omega_d = A/H$ is the dimensionless shear rate/amplitude, $\Omega = \omega_d/\omega_h$ is a frequency ratio and $\nu = v/(A\omega_d) = \nu_0/(\Gamma\Omega)$ a nondimensional swimming speed, with $\nu_0 = v/(\omega_h H)$. The Cartesian representation of (1-2), with Z measured from the bottom plate and XY the flow-vorticity plane (Fig. 1), was solved numerically to simulate a suspension of swimmers (see Supplementary Materials). The ratio R was computed from many simulations with a uniform distribution of initial swimmer orientations.

Non-swimmers ($\nu = 0$) passively follow the imposed oscillatory flow. In the absence of flow, the governing equations predict helical trajectories: $\mathbf{p}$ rotates around $\mathbf{n}$ (the helix axis) with frequency ω_h. With the experimental resonance close to helical swimming frequency, it is tempting to think that helical trajectories are responsible for the observed alignment. This is only partially true, as we shall see.

First we ask if the combination of 'non-helical' swimming and oscillatory shear alone is sufficient to induce ordering in experiment. Fig. 4 displays the ordering ratio (experiment a,b; simulation c,d) and simulated swimmer trajectories (e) for a model where helical swimming is switched off (dashed lines). While R peaks at characteristic values of the driving amplitude Γ (Fig 4c), it is entirely independent of driving frequency (Fig 4d) in stark contrast to the experiments. The non-helical limit does, however, predict alignment: it is worth considering further. When $\beta = 0$, the governing equations simplify considerably if we choose Euler angles Θ and Φ (Fig. 1c) such that $\mathbf{p} = \mathbf{n} = (\sin\Theta\sin\Phi, \cos\Theta, \sin\Theta\cos\Phi)$, where Θ increases from the direction of vorticity, $\mathbf{e}_y$, along the Y-axis, and Φ is measured from the Z-axis [e.g. $(\Theta, \Phi) = (\pi/2, \pi/2)$ is along the X-axis]. Equations (1-2) give

$$\dot{X} = \nu_\perp \sin\Phi + \Gamma\cos(t)Z \tag{3}$$

$$\dot{Y} = \nu_\parallel \tag{4}$$

$$\dot{Z} = \nu_\perp \cos\Phi \tag{5}$$

$$\dot{\Theta} = 0; \;\; \dot{\Phi} = \frac{\Gamma}{2}\cos(t) \tag{6}$$

where $\nu_\perp = \nu\sin\Theta_0$ and $\nu_\parallel = \nu\cos\Theta_0$ are the nondimensional swimming speed components perpendicular and parallel to $\mathbf{e}_y$. Integration of (4) and (6) yields $Y(t) = Y_0 + \nu_\parallel t$, $\Theta(t) = \Theta_0$ and

$$\Phi(t) = \Phi_0 + \frac{\Gamma}{2}\sin(t). \tag{7}$$

(Recall that $\Gamma = A/H$ is the non-dimensional shear rate.) As the Y component of the trajectory grows linearly in time, independent of shear, alignment can only depend on the coupled X and Z dynamics. In particular, closed orbits in the XZ-plane are present at resonance, see Fig. 4e, panel (i). For such orbits, progress only in the Y-direction is possible, leading to alignment. Off-resonance, orbits are open and cells can progress in X and Z directions (Fig. 4e, panel (ii)).

This phenomenology can be understood in terms of oscillatory Jeffery dynamics of the swimmer orientation. We see from (7) that oscillatory shear forces swimmer orientation in the vertical XZ-plane to describe circular arcs swept sinusoidally in time (contrast this with circular Jeffery orbits in steady shear flow, $\omega_d \to \infty$), with angular amplitude $\Gamma/2$. Folded orbits only arise when shear is sufficiently large to rotate swimmer orientation by integral multiples of π, so it can make no net progress during a cycle (see 4e). This provides a prediction for the resonant ordering amplitude $\Gamma_{\text{res}} \approx 2\pi n$, $n \in \mathbb{Z}$, in good agreement with non-helical simulations (Fig 4c). The latter agree qualitatively with the experimental results in Fig 4a. Quantitatively, much smaller values of Γ are sufficient to induce ordering in experiment. A possibility is that the Γ reported underestimates the shear rate swimmers were exposed to, e.g. because the intrinsic

flagellar beats cause effective cell shape changes leading to unexpected response to shear [29, 30]. Alternatively, additional mechanisms, such as those discussed below, may modify the ordering dynamics.

The model for non-helical swimmers predicts alignment as a function of amplitude, but does not reproduce the experimentally observed dependence on both driving amplitude *and* frequency (Fig 4b). *D. salina* is a helical swimmer, rotating at $1.5 - 2$ Hz [25]. This second, internal frequency provides the possibility of further resonance. Indeed, with $\beta \neq 0$ (recall β is the angle between $\mathbf{p}$ and $\mathbf{n}$) numerical results reveal that ordering is frequency dependent (Fig. 4d). Position equations are unchanged, but depend on more complex orientation dynamics resulting from the coupling of flow-induced and helical rotation. Cell orientation angles Θ_p and Φ_p, defining $\mathbf{p}$, evolve according to (see Supplementary Materials)

$$\dot{\Theta}_p = \Omega^{-1} \sin\Theta_n \sin(\Phi_n - \Phi_p), \tag{8}$$

$$\dot{\Phi}_p = \frac{\Gamma}{2} \cos(t) \tag{9}$$
$$+ \Omega^{-1} [\cos\Theta_n - \sin\Theta_n \cot\Theta_p \sin(\Phi_n + \Phi_p)],$$

whereas angles for $\mathbf{n}$ satisfy (6), such that $\dot{\Theta}_n = 0$, $\dot{\Phi}_n = \Gamma\cos(t)/2$. As the $\mathbf{p}$-dynamics are slaved to the $\mathbf{n}$-dynamics, trajectories with helical swimming do retain broad features of non-helical orbits in oscillatory shear, see Fig. 4e, but they are nevertheless qualitatively perturbed (even for infinitesimal β). Thus only for particular driving frequencies and amplitudes does helical swimming produce alignment-inducing orbits. The frequency condition for ordering can be obtained by considering the case of a swimmer with $\mathbf{n}$ in the direction of vorticity: $\Theta_n(0) = 0 = \Phi_n(0)$; $\Theta_p(0) = \beta$; and $\Phi_p(0) = 0$. Equation (9) then integrates to $\Phi_p(t) = \frac{\Gamma}{2}\sin(t) + \Omega^{-1}t$: a helical phase can perturb simple Jeffery rotation by the flow. Only when $\Omega \sim 1$, i.e. when the driving and helical phase are synchronised, can a resonant value of Γ give alignment, agreeing with both simulations and experiments (Fig 4b,d).

Oscillatory Jeffery orbits and helical swimming provide a first order explanation for the dependence of resonance in experiments on both frequency and amplitude. The model is predictive: helical frequency shifts alter resonant alignment, e.g. simulations of the predatory dinoflagellate *Pfiesteria piscida* (Supplementary Materials) predict a resonant frequency shift when helical frequency increases in the presence of prey (Fig 4d, inset). This description could be extended to investigate how additional effects such as taxes, orientation noise, inertia and cell shape either dominate, compete or act in concert with helical swimming to affect resonance. Intriguing possibilities include stochastic resonance due to noise in the flow velocity gradients [31] and the aforementioned effective shape due to flagellar beats [29, 30]. The possibility of flagellar deformation by shear [2] seems unlikely. Shear
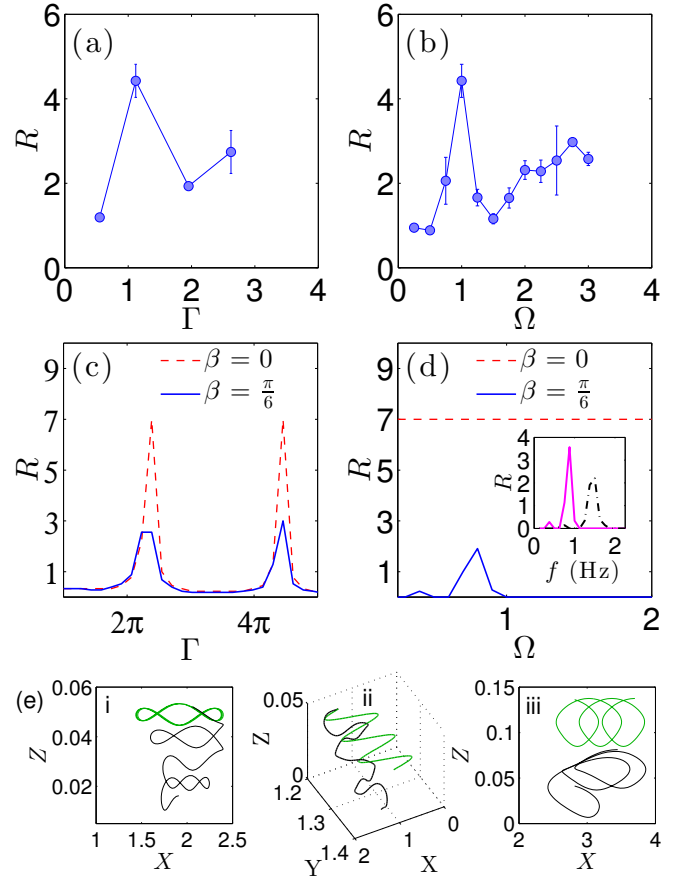

FIG. 4. Alignment ratio R vs. amplitude Γ and frequency Ω from experiment (errorbars smaller than data points not shown) (a, b) and simulation (c, d). Simulation predictions are shown with ($\beta = \pi/6$, solid) and without ($\beta = 0$, dashed) helical swimming (frequency $f_h = 2$Hz), only the latter providing frequency dependence. Trajectories ($\beta = 0$, green; $\beta = \pi/6$, black) are also shown in (e): at resonance, $[\Gamma, \Omega] = [7.5, 0.75]$, for XZ plane (i) and 3D views (ii); off-resonance $[\Gamma, \Omega] = [4, 0.75]$ (iii). Only trajectories closed in XZ provide ordering. Inset of (d): simulations of *P. piscida* in oscillatory flow, which increases its helical frequency from 1 (solid line) to 2 Hz (dash dot) when predating [33]. We predict a measureable shift in the resonance peak.

rates on the same order as our experiments can modify flagellar dynamics for cells held on a micropipette [32]. However, our cells are in suspension (free to rotate): much larger shear will be necessary to deform their flagella. A full analytical investigation of the nonlinear dynamics of the helical model in oscillatory shear is beyond the scope of this paper, but it is clear that much is to be discovered, analogous to structures observed for swimming cells in Poiseuille flow [15].

Conclusions. We have demonstrated the surprising response of swimming microalgae to oscillatory shear flows, producing an alignment of trajectories with a set of resonance peaks in the parameter space of driving frequency and amplitude. A simple model combining shear and

non-helical swimming predicts resonant alignment of the trajectories of swimming cells, but only when helical swimming is included does the experimentally observed frequency dependence of the resonance arise. The rich dynamics and the counterintuitive interactions between swimmers and flow revealed by our experiments and modelling have implications for both active suspension rheology and the design of novel cell processing methods. While simplified models of swimmers (rod or spheroidal pushers and pullers with no helical motion) appear adequate to explain active rheological phenomena such as shear-thickening in algal suspensions [17, 34], the current work suggests such models may fail in active *oscillatory* rheology experiments. Biotechnologically, the results hint at methods for improvement in efficiency of the algal processing pipeline [35]. For example, in downstream processing of useful microalgae, like the β-carotene producer *D. salina*, cells commonly experience oscillatory flows. Resonant alignment will provide boundary accumulation over times L/v, where L is the size of the shear plate and v is the swimming speed. This may be 'engineered out' by tuning process parameters from resonance; or it may be fruitfully exploited as a new way to guide and harvest cells.

SUPPLEMENTARY MATERIALS

Shear effects on swimming and flow

In order to establish that the swimming of *Dunaliella salina* in the absence of flow was not affected by exposure to oscillatory shear, the trajectory orientation and swimming statistics of cells were monitored before and after every shearing experiment, see Figure (5). Isotropy and mean speed return to normal once the oscillatory flow is halted. The only effect is a drop in the total number of swimmers in the field of view, probably a result of cell loss in the field of view generated by the anisotropic migration caused by the oscillatory shear (as discussed in the conclusions of the main text). The same (5) shows the simultaneous tracking of swimming algae and PEGylates polystyrene colloids, verifying they passively follow the flow, as expected.

Simulation model

As mentioned in the main text, mechanisms for the experimental trajectory ordering of *Dunaliella salina* in oscillatory shear flows were explored by numerical simulations of helical swimmers. The equations of motion of a swimmer were based on a recently proposed model by Bearon [28]. In this model (notation as in the main text), cell position $\mathbf{r}$ evolves by swimming with mean speed v along the direction $\mathbf{p}$. Through an intrinsic torque due to nonplanar swimming the cell also generates rotation about a direction $\mathbf{n}$. The dynamics of swimmers in a flow $\mathbf{u}$ is governed by

$$\dot{\mathbf{r}} = \mathbf{u} + v\mathbf{p} \qquad (A.10)$$

$$\dot{\mathbf{p}} = \boldsymbol{\omega}_c \times \mathbf{p} \qquad (A.11)$$

$$\dot{\mathbf{n}} = \boldsymbol{\omega}_c \times \mathbf{n} \qquad (A.12)$$

where the angle between $\mathbf{p}$ and $\mathbf{n}$ is fixed and given by $\mathbf{p} \cdot \mathbf{n} = \cos\beta$ and $\boldsymbol{\omega}_c$ is the net angular velocity of a cell resulting from the balance of torques on it. Bearon considered external torques on the cells due to gravity on bottom heavy spherical swimmers in a flow, so that $\boldsymbol{\omega}_c = \omega_g \mathbf{p} \times \mathbf{e}_z + \omega_h \mathbf{n} + \frac{1}{2}\boldsymbol{\omega}$, where ω_g is the gravitational reorientation frequency, ω_h is the intrinsic angular speed of helical rotation and ω is the flow vorticity (horizontal and vertical linear shear flows were solved for in [28]). The model neglects known effects, such as cell shape and stochastic reorientation. These could easily be included (e.g. as in [7]), but to capture a minimal mechanism for our observations we neglect them here, and additionally neglect gravitational torques. These torques will only act on cells swimming with a significant vertical component. For these, gravitational reorientation of the cells acts on timescales $1/\omega_g \sim 10$s [36], which are large compared to the flow timescales for most driving frequencies considered. Thus, flow reorientation is expected to dominate the dynamics, as verified from simulations (see Figure 6).

We then assume the simple oscillatory flow $\mathbf{u}(t) = \dot{\gamma}_\infty Z \cos(\omega_d t)\mathbf{e}_x$ (vorticity $\boldsymbol{\omega}(t) = \dot{\gamma}_\infty \cos(\omega_d t)\mathbf{e}_y$), where $\dot{\gamma}_\infty = \omega_d A/H$ is the maximum shear rate for driving angular frequency $\omega_d = 2\pi f_d$ and amplitude A. Nondimensionalising in terms of these time $(1/\omega_d)$ and length (H) scales, equations (A.10-A.12) reduce to equations (1) and (2) of the main text

$$\dot{\mathbf{r}} = \Gamma \cos(t) Z\mathbf{e}_x + \nu\mathbf{p} \qquad (A.13)$$

$$\dot{\mathbf{p}} = \left[\frac{\Gamma}{2} \cos(t)\mathbf{e}_y + \Omega^{-1}\mathbf{n}\right] \times \mathbf{p} \qquad (A.14)$$

$$\dot{\mathbf{n}} = \frac{\Gamma}{2} \cos(t)\mathbf{e}_y \times \mathbf{n} \qquad (A.15)$$

where, as in the main text, we define the dimensionless driving amplitude/shear rate $\Gamma = A/H$ and frequency $\Omega = \omega_d/\omega_h$. The parameter $\nu = v/(A\omega_d)$
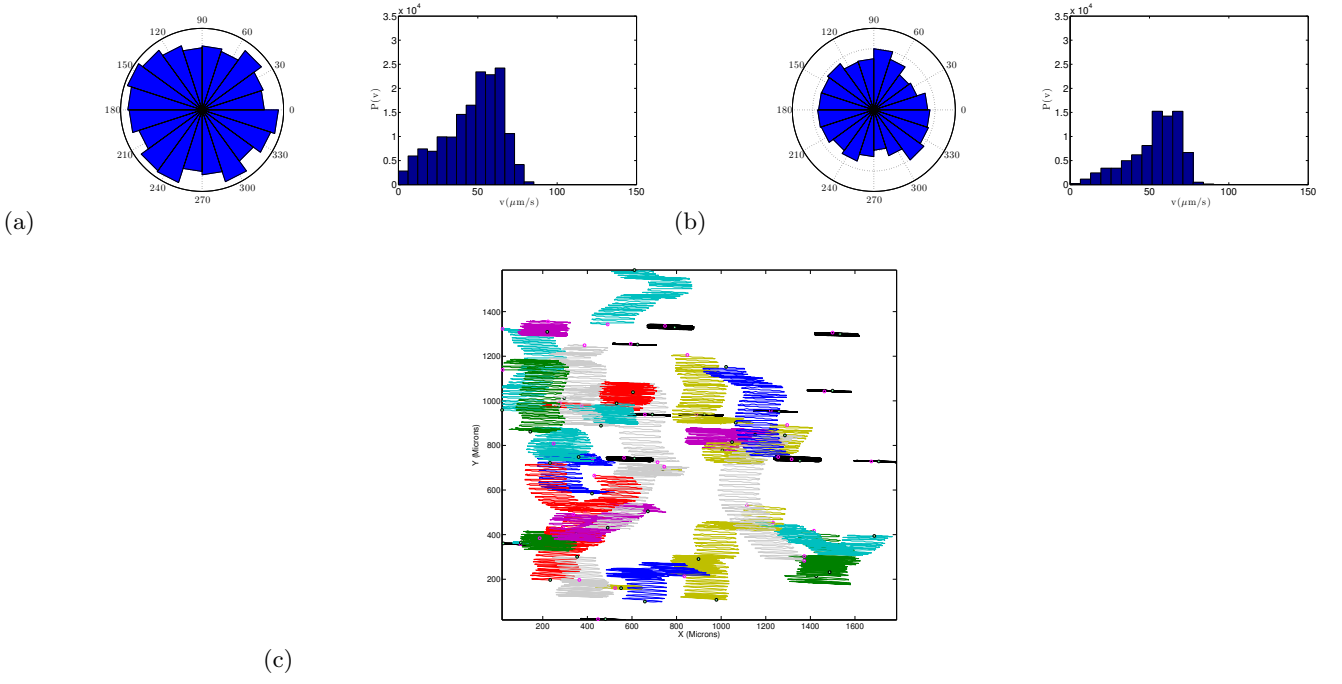
(a)

(b)

(c)

FIG. 5. Trajectory orientation and speed PDFs before (a) and after (b) oscillatory flow ($A = 224\ \mu$m, $f = 2$ Hz as in figure 2c of main text). When oscillatory shear ceases, trajectory isotropy is recovered. (c) Swimmer trajectories (colour) and colloids (black) for $A = 150\ \mu$m, $f = 2$ Hz. The latter passively follow the oscillatory flow.

gauges the relative magnitude of advection by swimming to advection by flow. Re-writing $\nu = \nu_0/\Omega\Gamma$, with $\nu_0 = v/(H\omega_h)$ a constant, we see that ν cannot be varied independently of the dimensionless driving parameters. In [28], where gravity can play a significant role, the ODEs for the components of (A.13), (A.14) and (A.15) were derived in a Cartesian coordinate frame where Euler angles are defined with respect to the vertical. We consider instead a Cartesian frame with Euler angles Θ and Φ describing the helical rotation direction defined from the vorticity direction $\mathbf{e}_y$ along the Y-axis: $\mathbf{n} = (\sin\Theta_n \sin\Phi_n, \cos\Theta_n, \sin\Theta_n \cos\Phi_n)$, as described in the main text and shown in Fig. 1c of the main text. This choice simplifies the angular equations of motions and makes the dynamics more physically transparent. The equations of motion for the swimmers then become

$$\dot{X} = \nu \sin\Theta_p \sin\Phi_p + \Gamma\cos(t)Z \qquad (\text{A.16})$$

$$\dot{Y} = \nu \cos\Theta_p \qquad (\text{A.17})$$

$$\dot{Z} = \nu \sin\Theta_p \cos\Phi_p \qquad (\text{A.18})$$

$$\dot{\Theta}_n = 0;\ \ \dot{\Phi}_n = \frac{\Gamma}{2}\cos(t) \qquad (\text{A.19})$$

$$\dot{\Theta}_p = \Omega^{-1}\sin\Theta_n \sin(\Phi_n - \Phi_p) \qquad (\text{A.20})$$

$$\dot{\Phi}_p = \Gamma\cos(t)/2 + \Omega^{-1}\cos\Theta_n$$
$$\qquad - \Omega^{-1}\sin\Theta_n \cot\Theta_p \sin(\Phi_n + \Phi_p) \qquad (\text{A.21})$$

When $\beta = 0$, helical effects are negligible. In this limit, losing subscripts and defining $\nu_\perp = \nu \sin\Theta_0$,
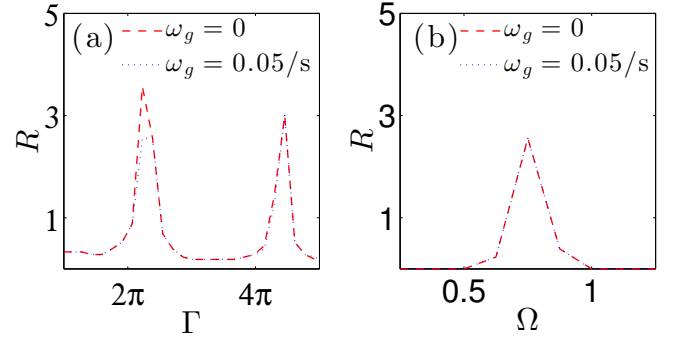

FIG. 6. Alignment ratio simulations with and without gravitaxis, which makes little difference to ordering dominated by flow and helical contributions.

$\nu_\parallel = \nu \cos\Theta_0$, equations (A.16–A.21) reduce to equations (3−6) in the main text, where the dynamics for Θ, Φ and Y are trivially solved for analytically. The non-integrable equations of system (A.16–A.21) for swimming cells were solved numerically with MATLAB (Mathworks, Natick, MA, USA) using a Runge-Kutta-Fehlberg (RK45) method in a periodic box of size $L_x \times L_y \times L_z$, where $L_x = L_y = 18$ and $L_z = 1$, recalling all lengths are rescaled by the gap width $H = 400\mu$m. Realistic $D.\ salina$ mean swimming parameters (along-helix speed $v = 80\mu$m/s and intrinsic frequency $f_d = 2$Hz) were used [25], ignoring phenotypic variations across the population. The helical angle between the swim-

ming direction $\mathbf{p}$ and the helical axis of rotation $\mathbf{n}$ can be estimated from $\beta = \arccos(v/v_p) = 0.5$, where $v_p = 60\mu$m/s is the mean progressive speed along the helical axis [25]. Simulations were also carried out for the oscillatory flow response of the predatory dinoflagellate *Pfiesteria piscida*. The swimming parameters for this dinoflagellate, helix radius r_h, frequency f_h and along-helix speed v, have been recently characterised using digital holographic microscopy [33]. It was observed that *P. piscida* modifies its helical swimming from $[r_h, f_h, v] = [9.6\mu$m, 1.1Hz, 174μm/s] in the absence of prey, to $[r_h, f_h, v] = [11.4\mu$m, 1.9Hz, 240μm/s] when prey is present. Our prediction for this change in helical swimming is shown in the inset of Fig. 4d of the main text. The helical angle used in simulations was found from these parameters from $\beta = \arcsin(\omega_h r_h/v)$, where $\omega_h = 2\pi f_h$. In all simulations, swimmers were set off at $Z = 1/2$, with initial values of $\mathbf{p}$ 2D-isotropic in the horizontal plane and $\mathbf{n}$ to be rotated by β out of the plane. The following realistic driving parameters were used: $\Omega = 0.25$-3 ($f_d = 1$-6Hz) and $\Gamma = 0.125$-8.75 ($A = 50$-14000μm). The ordering ratios R were obtained from the simulation position data, as for experiments.

* oac24@cam.ac.uk

[1] T. J. Pedley and J. O. Kessler, Annu. Rev. Fluid Mech. **24**, 313 (1992).
[2] R. Rusconi and R. Stocker, Curr. Opin. Microbiol. **25**, 1 (2015).
[3] W. M. Durham, J. O. Kessler, and R. Stocker, Science **323**, 1067 (2009).
[4] M. A. Bees and O. A. Croze, Biofuels **5**, 53 (2014).
[5] N. A. Hill and T. J. Pedley, Fluid Dyn. Res. **37**, 1 (2005).
[6] R. Bearon, M. A. Bees, and O. A. Croze, Phys. Fluids (2012).
[7] O. A. Croze, G. Sardina, M. Ahmed, M. A. Bees, and L. Brandt, J. R. Soc. Interface **10**, 20121041 (2013).
[8] W. M. Durham, E. Climent, M. Barry, F. D. Lillo, G. Boffetta, M. Cencini, and R. Stocker, Nat. Commun. **4**, 3148 (2013).
[9] C. Zhan, G. Sardina, E. Lushi, and L. Brandt, J. Fluid Mech. **739**, 22 (2014).
[10] F. De Lillo, M. Cencini, W. M. Durham, M. Barry, R. Stocker, E. Climent, and G. Boffetta, Phys. Rev. Lett. **112**, 044502 (2014).
[11] O. A. Croze, E. E. Ashraf, and M. A. Bees, Phys. Biol.

7, 046001 (2010).
[12] Y. Hwang and T. J. Pedley, J. Fluid Mech. **738**, 522 (2014).
[13] X. Garcia, S. Rafaï, and P. Peyla, Phys. Rev. Lett. **110**, 138106 (2013).
[14] C. R. Willams and M. A. Bees, J. Fluid Mech. **678**, 41 (2011).
[15] A. Zöttl and H. Stark, Phys. Rev. Lett. **108**, 218104 (2012).
[16] A. Sokolov and I. S. Aranson, Phys. Rev. Lett. **103**, 148101 (2009).
[17] S. Rafaï, L. Jibuti, and P. Peyla, Phys. Rev. Lett. **104**, 098102 (2010).
[18] A. Chengala, M. Hondzo, and J. Sheng, Phys. Rev. E **87**, 052704 (2013).
[19] U. Pick, L. Karni, and M. Avron, Plant Physiol. **81**, 92 (1986).
[20] J. Polle, private communication.
[21] V. A. Martinez, R. Besseling, and O. A. C. *et al.*, Biophys. J. **103**, 1637 (2012).
[22] M. Kilfoil lab software research tools `http://people.umass.edu/kilfoil/downloads.html`.
[23] J. Crocker and D. G. Grier, J. Colloid Interface Sci. **179**, 298 (1996).
[24] N. A. Hill and D.-P. Häder, J. Theor. Biol. **186**, 503 (1997).
[25] O. A. Croze *et al.*, in preparation.
[26] K. V. Mardia and P. Jupp, *Directional Statistics* (John Wiley and Sons, 2000).
[27] K. W. Foster and R. D. Smyth, Microbiol. Rev. **44**, 572 (1980).
[28] R. N. Bearon, J. Math. Biol. **66**, 1341 (2013).
[29] S. O'Malley and M. A. Bees, Bull. Math. Biol. **74**, 232 (2012).
[30] L. Jibuti, W. Zimmermann, S. Rafaï, and P. Peyla, ArXiv preprint (2014).
[31] F. Guzmán-Lastra and R. Soto, Phys. Rev. E **86**, 037301 (2012).
[32] G. S. Klindt, C. Ruloff, C. Wagner, and B. M. Friedrich, ArXiv preprint (2016).
[33] J. Sheng, E. Malkiel, J. Katz, J. Adolf, R. Belas, and A. R. Place, Proc. Natl. Acad. Sci. USA **104**, 17512 (2007).
[34] M. C. Marchetti, J. F. Joanny, T. B. Liverpool, J. Prost, M. Rao, and R. A. Simha, Rev. Mod. Phys. **85**, 1143 (2015).
[35] S. A. Scott, M. P. Davey, J. S. Dennis, I. Horst, C. J. Howe, D. J. Lea-Smith, and A. G. Smith, Curr. Opin. Biotechnology **21**, 277 (2010).
[36] O. A. Croze, R. N. Bearon, and M. A. Bees, in preparation.